SAND2022-14458

SANDIA REPORT
SAND20XX-XXXX
Printed Click to enter a date

Sandia National Laboratories

Computational Fluid Dynamics and Heat Transfer Modeling of a Dimpled Heat Exchanger

Sal Rodriguez, Graham Monroe, and Amy Chen

Prepared by
Sandia National Laboratories
Albuquerque, New Mexico
87185 and Livermore,
California 94550

Issued by Sandia National Laboratories, operated for the United States Department of Energy by National Technology & Engineering Solutions of Sandia, LLC.

Available to DOE and DOE contractors from
U.S. Department of Energy
Office of Scientific and Technical Information
P.O. Box 62
Oak Ridge, TN 37831

Telephone: (865) 576-8401
Facsimile: (865) 576-5728
E-Mail: reports@osti.gov
Online ordering: http://www.osti.gov/scitech

Available to the public from
U.S. Department of Commerce
National Technical Information Service
5301 Shawnee Rd
Alexandria, VA 22312

Telephone: (800) 553-6847
Facsimile: (703) 605-6900
E-Mail: orders@ntis.gov
Online order: https://classic.ntis.gov/help/order-methods/

ABSTRACT

Multiphysics and analytical calculations were conducted for a heat exchanger with passive, natural circulation flow. A glycol/water working fluid convects the heat to a dimpled heat exchanger shell, which subsequently transfers the heat to the soil, which acts as the ultimate heat sink. Because the system is fully-passive, it is not subject to the expenses, maintenance, and mechanical breakdowns associated with moving parts.

Density, heat capacity, and thermal conductivity material properties were measured for various soil samples, and subsequently included as input for the soil heat conduction model. The soil model was coupled to a computational fluid dynamics (CFD) heat exchanger model that included the dynamic Smagorinsky large eddy simulation and k-omega turbulence models. The analysis showed that the fluid dynamics and heat transfer models worked properly, albeit at a slow pace. Nevertheless, the coupled CFD/heat conduction simulation ran long enough to determine a key parameter—the amount of heat conducted from the heat exchanger to the ground. This unique performance value, along with experimental data, was used as input for stand-alone, fast-running CFD models, as well as boundaries to obtain solutions to partial differential equations for soil heat conduction.

CONTENTS

1. Introduction 9
2. Experimental Data 12
   2.1. Soil Material Properties Experimental Data 12
   2.2. Temperature Experimental Data 13
3. System Models and Computational Output 15
   3.1. CFD Model Coupled with Heat Conduction (Multiphysics) 15
   3.2. Stand-Alone CFD Model with Multiphysics Heat Flux Boundary 20
   3.3. Soil Temperature Distribution Based on Analytical Heat-Conduction Solutions 23
4. Miscellaneous Recommendations Regarding Corrosion and Turbulent Forced Flow vs. Natural Circulation 28
   4.1. Recommendations to Reduce Corrosion 28
   4.2. Recommendations Regarding Forced vs. Natural Circulation 28
5. Summary, Conclusions, and Recommendations 31
6. References 32
Distribution 34

LIST OF FIGURES

Figure 1-1. Conceptual schematic of house and greenhouse applications for the fully-passive, dimpled heat exchanger system. 9
Figure 1-2. 2A. Patrick Johnson inside a ground cavity that was excavated for the dimpled heat exchanger. 2B. Full-scale, fully-passive, dimpled heat exchanger. 2C. Heat exchanger lowered into the soil. 2D. Surface zoom showing the dimples that provide enhanced heat transfer. 10
Figure 2-1. Average air and ground temperature. 14
Figure 3-1. Multiphysics CFD/heat conduction heat exchanger and ground model. 15
Figure 3-2. Top view for the Multiphysics CFD/heat conduction heat exchanger and ground model. 16
Figure 3-3. Fuego vs. Aria boundary temperature range. 17
Figure 3-4. Fuego vs. Aria computational temperature range. 17
Figure 3-5. Fuego vs. Aria convective heat transfer coefficient range. 18
Figure 3-6. Multiphysics-calculated transient heat flux. 19
Figure 3-7. Side view of the dimpled heat exchanger. 20
Figure 3-8. Top view of the dimpled heat exchanger. 20
Figure 3-9. Stand-alone CFD simulation showing the calculated pressure distribution. 21
Figure 3-10. Stand-alone CFD simulation showing the calculated fluid velocity distribution. 22
Figure 3-11. Stand-alone CFD simulation showing the calculated fluid temperature distribution. 22
Figure 3-12. PDE solution for the soil temperature distribution as a function of radial distance *r*. 27

LIST OF TABLES

Table 2-1. Physical and thermal properties of the soil samples. 12

This page left blank

ACRONYMS AND DEFINITIONS

Abbreviation	Definition / Units (if applicable)
A	Surface area (m^2)
BC	boundary condition
CFD	computational fluid dynamics
C_P	heat capacity at constant pressure (J/kg-K)
g	gravitational constant
Gr	Grashof number (a measure of natural convection)
GH	greenhouse
H	height (m)
IC	initial condition
k	thermal conductivity (W/m-K)
LES	large eddy simulation
N	number of parallel processors
Nu	Nusselt number (a measure of natural convection)
PDE	partial differential equation
Pr	Prandtl number (the ratio of the fluid viscous vs. thermal properties)
$\dot{q}''$	heat flux per unit area and time (W/m^2)
$\dot{q}'''$	heat flux per unit volume and time (W/m^3)
r	radial coordinate
R	radial distance (m)
Ra	Rayleigh number (a measure of natural circulation that includes *Pr*)
RANS	Reynolds-averaged Navier Stokes
Re	Reynolds number (a measure of the forced circulation)
SS	steady state
T	temperature (K, °C, and °F)
t	time (s)
u	velocity (m/s)
x_{char}	characteristic length (m)
Greek	
α	thermal diffusivity (m^2/s)

Abbreviation	Definition / Units (if applicable)
β	fluid volume expansion coefficient (1/K)
ρ	density (kg/m^3)
μ	dynamic viscosity (kg/m-s)
ν	kinematic viscosity (m^2/s)

1. INTRODUCTION

This work extended the modeling and simulations that were conducted in 2020 for a novel, dimpled heat exchanger for home and greenhouse cooling applications. The heat exchanger extracts heat from a home or greenhouse using a glycol/water mixture as the working fluid. The heat is then passively convected via natural circulation to a concentric, dimpled cylindrical heat exchanger. The dimpling pattern increases the degree of fluid mixing, and hence, the amount of heat transfer. The heat is thereafter conducted to the soil, which provides the ultimate heat sink.

Beachhead applications for the passive, dimpled heat exchanger include house and greenhouse utilization, as shown conceptually in Figure 1-1. Figure 1-2 provides additional details for the ground cavity associated with the dimpled heat exchanger. The blue pipes shown in Figure 1-2B transfer the glycol/water working fluid to and from the cooled structure.

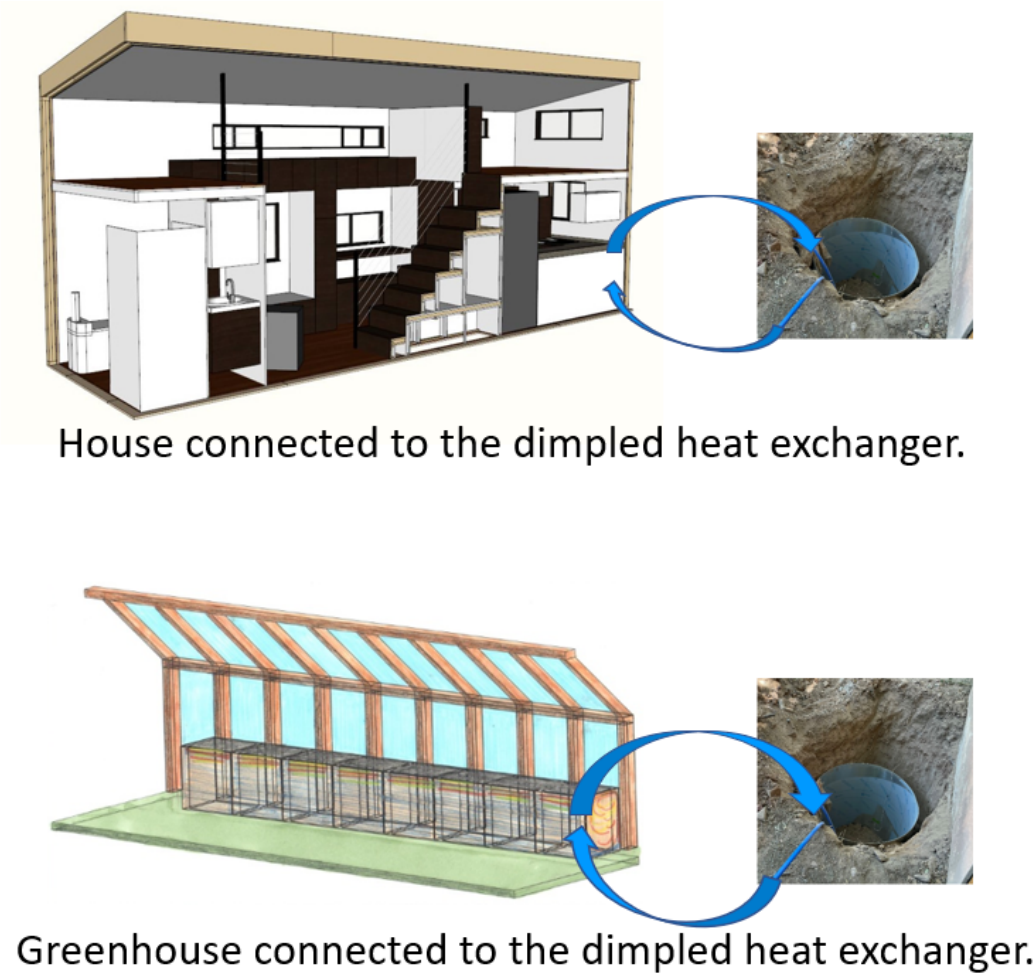

Figure 1-1. Conceptual schematic of house and greenhouse applications for the fully-passive, dimpled heat exchanger system.

Figure 1-2. 2A. Patrick Johnson inside a ground cavity that was excavated for the dimpled heat exchanger. 2B. Full-scale, fully-passive, dimpled heat exchanger. 2C. Heat exchanger lowered into the soil. 2D. Surface zoom showing the dimples that provide enhanced heat transfer.

The following are of particular interest for this work phase:

- more prototypic modeling of the soil,
- the coupling of the computational fluid dynamics (CFD) with the heat conduction model of the soil,
- the more mechanistic application of heat transfer boundary conditions (BCs), and
- the overall system behavior dynamics and performance of the heat exchanger and the soil.

To obtain a more mechanistic and prototypic soil computational model, the density, heat capacity, and thermal conductivity material properties were measured for various soil samples. Moreover, soil temperature measurements were conducted by the lead

business point of contact and were compared with the calculations. The material properties and temperature experimental data are presented in Section 2.

For the present work, the stand-alone CFD model was extended by considering two turbulence models, the dynamic Smagorinsky large eddy simulation (LES) turbulence model and the 2006 k-omega Reynolds-averaged Navier Stokes (RANS) turbulence model. Both turbulence models are ideal for dimpled surfaces, curvature, wall effects, and low-Reynolds turbulence flow. The distinction between the two models is that the LES captures the spatial and dynamic eddy behavior, but requires more computational time, whereas the 2006 k-omega only captures the time-averaged behavior of the turbulent eddies, but at a faster computational time. In addition, a soil heat-conduction model was developed, and coupled onto the CFD model, which is referred as the Multiphysics model. The stand-alone and Multiphysics models are described in Section 3 and constitute the most prototypic models developed for this effort thus far. The section also describes the key modeling assumptions and computational results for all the Multiphysics and stand-alone models.

Section 3 also includes a discussion of several partial differential equations (PDEs) that were solved analytically using two different types of BCs, which were based on the output from the Multiphysics simulations.

Finally, some initial estimates regarding turbulent natural circulation vs. forced (pumped) circulation are included in Section 4. In particular, it was of interest to explore heat exchanger applications that involve higher heat loads, and thus require flow rates that exceed those of natural circulation.

2. EXPERIMENTAL DATA

The soil material properties are presented in this section, as well as the soil temperature measurements.

2.1. Soil Material Properties Experimental Data

Three soil samples were taken in Albuquerque by Sandia National Laboratories and taken to Daniel B. Stephens & Associates, Inc., to determine their physical and thermal properties. The upper sample was taken at a depth of approximately 0.3 m, while the two lower samples were taken at approximately 0.6 m.

Note that there are different ASTM standards [ASTM]; to avoid ambiguity, the following specific standards were used for the dry bulk density, while the ASTM D7263 and D2216 standards were used for the moisture content. The ASTM D7263 standard was used for the porosity. Finally, the ASTM D5334 standard was used for the thermal properties (e.g., heat capacity, thermal conductivity, and thermal diffusion). The measured physical and thermal properties data are summarized in Table 1.

Table 2-1. Physical and thermal properties of the soil samples.

Sample	Gravimetric Moisture Content (%)	Volumetric Moisture Content (%)	Dry Bulk Density (kg/m^3)	Temperature (K)	Thermal Conductivity (W/m-K)	Thermal Resistivity (K-m/W)	Heat Capacity at Constant Pressure (J/kg-K)	Thermal Diffusivity (m^2/s)
Upper 1	4.18	6.98	1,670	297.2	0.515	1.941	879.6	3.51×10^{-7}
Lower 1	5.68	9.24	1,630	297.7	0.655	1.526	1,301	3.09×10^{-7}
Lower 2	6.34	9.61	1,520	298.0	0.753	1.327	1,324	3.74×10^{-7}

Note that the thermal conductivity ranged from 0.515 to 0.753 W/m-K, which is consistent with the average ground thermal conductivity of 0.525 W/m-K noted by other researchers [Abu-Hamdeh and Reeder, 2000]. It is also noteworthy that the upper soil sample was visually different, both in color and composition, than the two lower samples. More specifically, the upper sample tended to have more sand and gravel, and had a lighter color, perhaps because it was associated with higher levels of caliche. Caliche is a tightly-packed sedimentary soil that is high in calcium carbonate, and is found extensively in New Mexico. Calcium carbonate ranges in color from white to yellow, acts as a binding material for the soil, and tends to impede the flow of water through soil. By contrast, the lower soil samples were less hardened, potentially indicating a lower quantity of caliche. The lower samples also tended to have less sand and gravel. Hence, the upper soil is not as prototypic as the lower soil samples where the heat exchanger is to be located.

Hence, the average of the lower soil samples was used for this modeling effort, given its more prototypic nature with respect to the soil adjacent to the heat exchanger. In this case, this assumption results in a thermal diffusivity of 3.42×10^{-7} m^2/s. Moreover, the measured results confirmed that the upper sample had a higher density, primarily due to the tight packing likely provided by the caliche. However, caliche acts more as an insulator as compared with the lower soil, so it is not surprising that the lower samples had a significantly higher thermal conductivity. *Hence, lower caliche concentrations in the ground benefit the heat transfer to the ground, and thus the performance of the passive heat exchanger.*

For the steel dimpled heat exchanger, it is assumed that it is based on a 1% carbon steel, which as a thermal conductivity of 43 W/m-K [Holman, 1990]. The material properties of the glycol/water working fluid are described in an earlier analysis [Rodriguez, Monroe, and Fort, 2020].

2.2. Temperature Experimental Data

The averaged air and ground temperature at diverse depths was recorded from March through August 2022 by Patrick Johnson, and is shown in Figure 2-1. While the ambient temperature ranged significantly from as low as approximately 50.5 °F (283.4 K) at night, to as high as 97.5 °F (309.5 K) during the day, the average air temperature ranged from 56 to 80 °F (286.5 to 299.8 K). Hence, because of the second law of thermodynamics, it is expected that the ground temperature will always be cooler than the ambient temperature, and it is also expected that the ground temperature will decrease as the ground depth increases, though at an asymptotic pace, with larger temperature drops initially, followed by decreased temperature drops further on. *This is principally what Figure 2-1 shows, with an asymptotic limit in the range of nine to 12 feet, and hence, digging a cavity that exceeds 12 feet is counterproductive.*

From Figure 2-1, it is evident that both the air and ground temperature approached an asymptotic peak, whereby the highest ambient and ground temperatures were reached. This, then, delineates the peak ground BCs against which the working fluid heat can be transferred. More specifically, the peak temperature at 3, 6, 9, and 12 feet (0.91, 1.83, 2.74, and 3.66 m) was approximately 78, 74, 69.5, and 63.5 °F, respectively (298.7, 296.5, 294.0, and 290.7 K). Hence, from a thermodynamic limit, these temperatures represent the maximum achievable glycol/water return temperature possible. In most cases, the addition of engineering inefficiencies will likely add approximately 2 to 4 °F (1.11 to 2.22 K) to these limits*. It is therefore expected that during the summer operational time period, the lowest-achievable temperature of the working fluid is approximately 65.5 to 67.5 °F (291.8 to 292.9 K). At this point, it is assumed that the heat exchanger top is insulated. Moreover, if the ground in the vicinity near the heat exchanger is shaded, then it is possible that the fluid temperature can be lowered by a few degrees. This could be achieved via a porch-like structure, or more simply, via a solar-reflective blanket over the ground.*

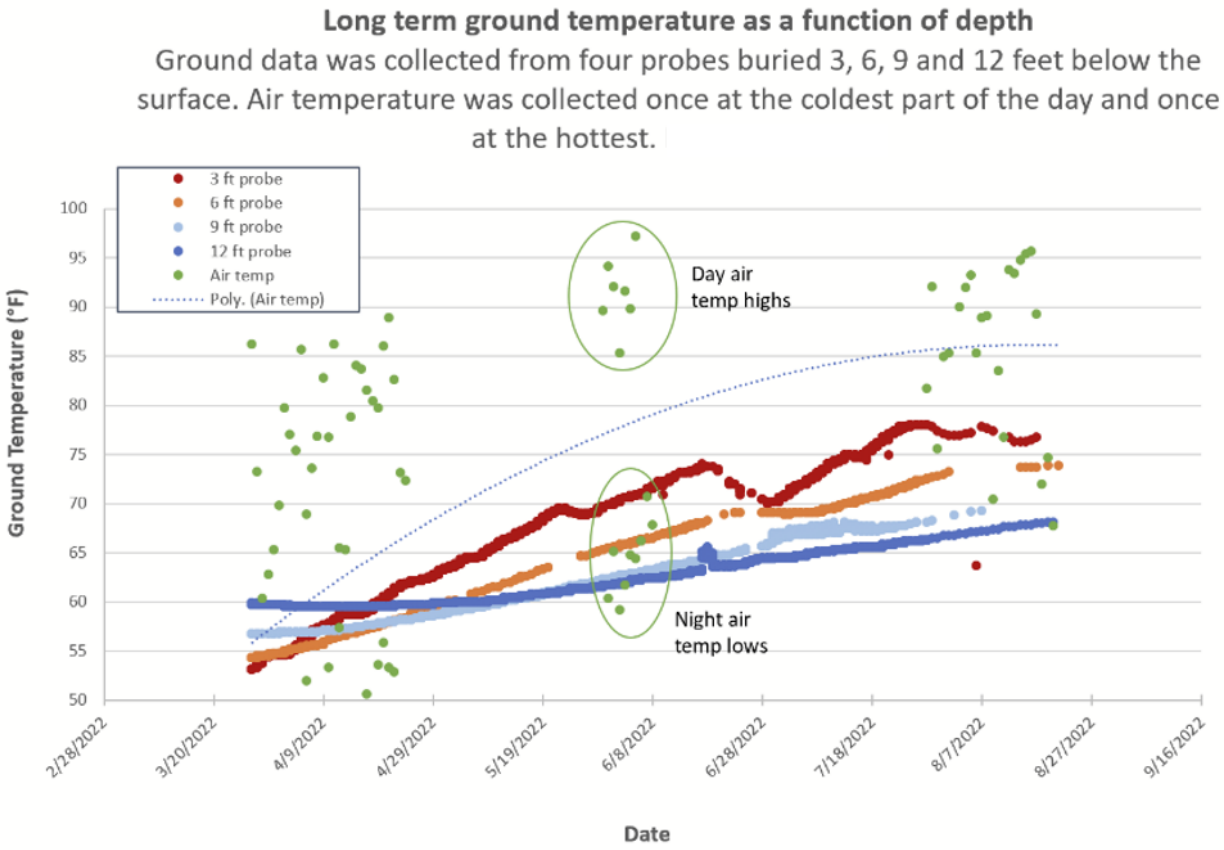

Figure 2-1. Average air and ground temperature.

3. SYSTEM MODELS AND COMPUTATIONAL OUTPUT

For this phase, the soil and metal jacket models were extended, to provide more prototypic heat transfer analysis. The stand-alone and Multiphysics models are fully transient and full-scale.

3.1. CFD Model Coupled with Heat Conduction (Multiphysics)

The Multiphysics simulation consisted of two domains: the exchanger (fluid computation via the Fuego CFD code) and the ground (solid heat conduction via the Aria code). The model and its BCs are shown in Figure 3-1. The mass flow inlet and outlet BCs are at the top and bottom of the gray cylinder, respectfully.

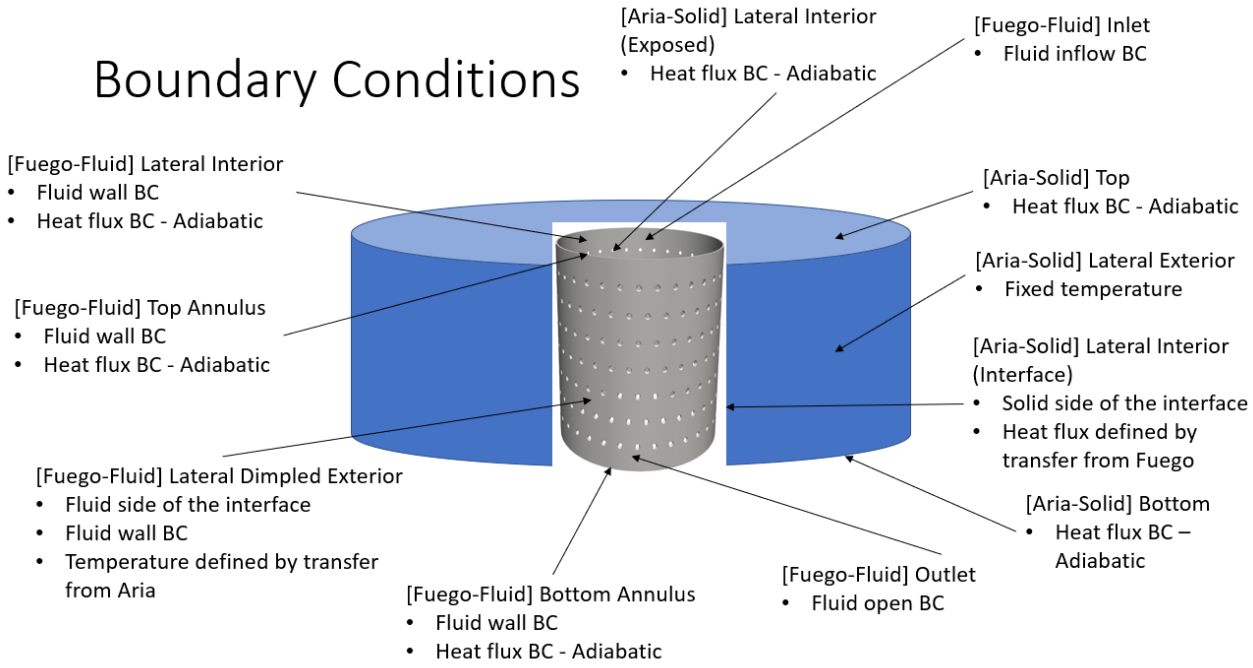

Figure 3-1. Multiphysics CFD/heat conduction heat exchanger and ground model.

Two Multiphysics models were generated: one with a dimpled heat exchanger and one with a dimple-free heat exchanger to compare their performance. Various boundaries were applied to investigate the overall behavior of the system. In one case, the ground was provided with a temperature gradient initial condition (IC) to approximate the steady state, and in another boundary sensitivity, a uniform cold temperature was imposed. The cold ground temperature was 55.1 °F (286.2 K), while the temperature of the hot fluid entering the exchanger was 125 °F (324.8 K).

The ground adjacent to the inner side of the heat exchanger was treated as an adiabatic boundary; it is therefore represented as a “void” in the top view illustration of the system, as shown in Figure 3-2.

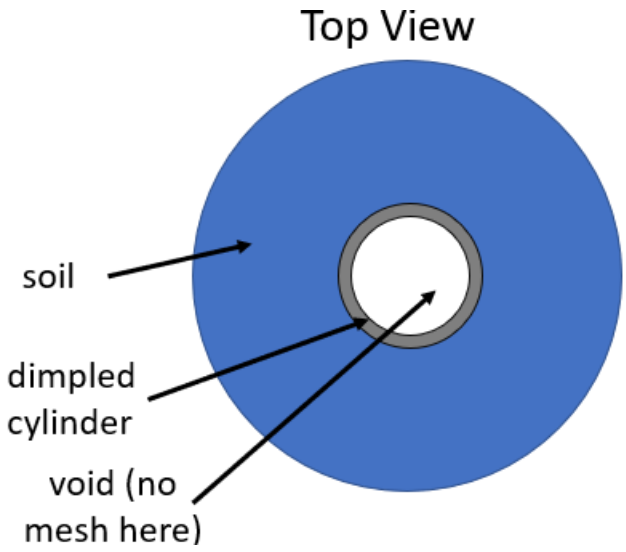

Figure 3-2. Top view for the Multiphysics CFD/heat conduction heat exchanger and ground model.

All simulations used a Dirichlet-convective heat transfer model at the fluid-solid interface, which applies a wall temperature from the solid (ground) region into the fluid (heat exchanger) region, advances the fluid region, linearizes the fluid heat flux into a convective-type expression, applies this linearized flux onto the solid region, and finally, advances the solid region. An alternative Dirichlet-Neumann heat transfer model, which differs in that it does not linearize the heat flux, was also tested for comparison. However, none of the final results provided in this document made use of this model, as this approach provided no additional output insights.

For the fluid simulations, the turbulence was resolved with the dynamic Smagorinsky LES and 2006 k-omega models using second-order implicit-time integration; the Boussinesq buoyancy model was activated to account for natural circulation. The ground solid region used the BDF2 time-integration numerical approach to model the heat conduction.

The fluids modeled were a 50%-50% propylene glycol-water mixture and 100% water. Density, dynamic viscosity, and enthalpy were modeled as piecewise functions of temperature from tables of reference data [Rodriguez, Monroe, and Fort, 2020]. For the current analysis, it was found that a linear relationship between enthalpy and temperature with a constant slope, as defined by specific heat capacity, was necessary for the Fuego enthalpy equation to converge; thus, the Fuego piecewise table was replaced with a linear approximation.

Comparisons of the transferred wall temperature and convection coefficient, as well as the general temperature fields, show good agreement between the two different physics regions at the fluid-solid interface at the dimple surface. This is shown in Figures 3-3 through 3-5, which show the boundary temperature, the computational temperature, and the convective heat transfer coefficient along a cross-section of the dimples, respectively.

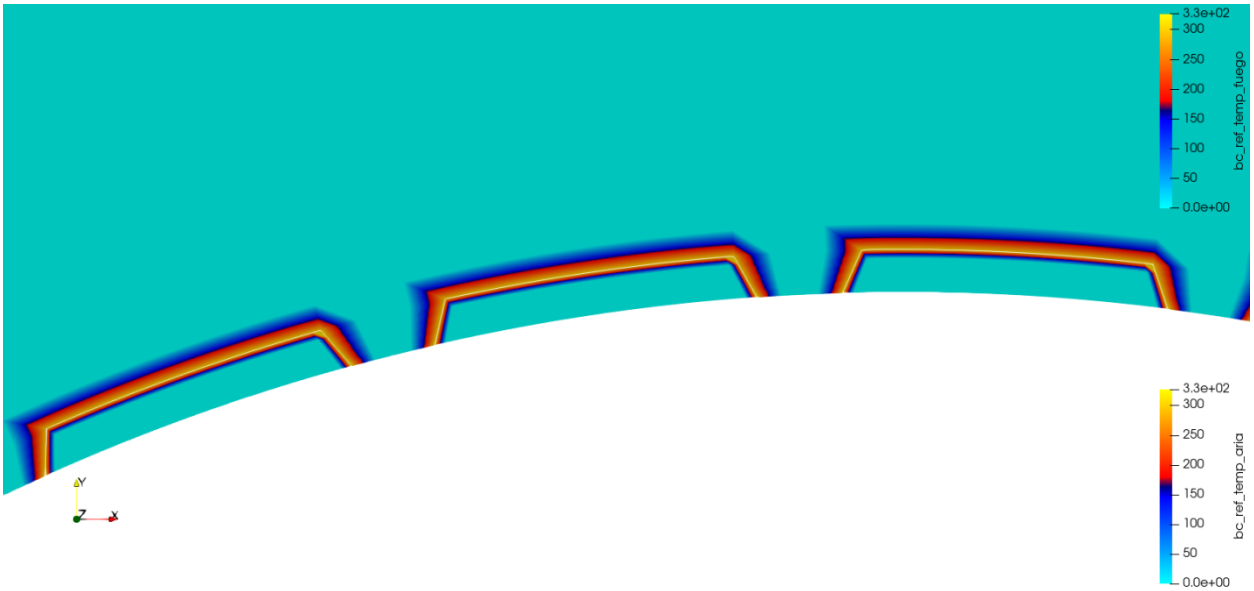

Figure 3-3. Fuego vs. Aria boundary temperature range.

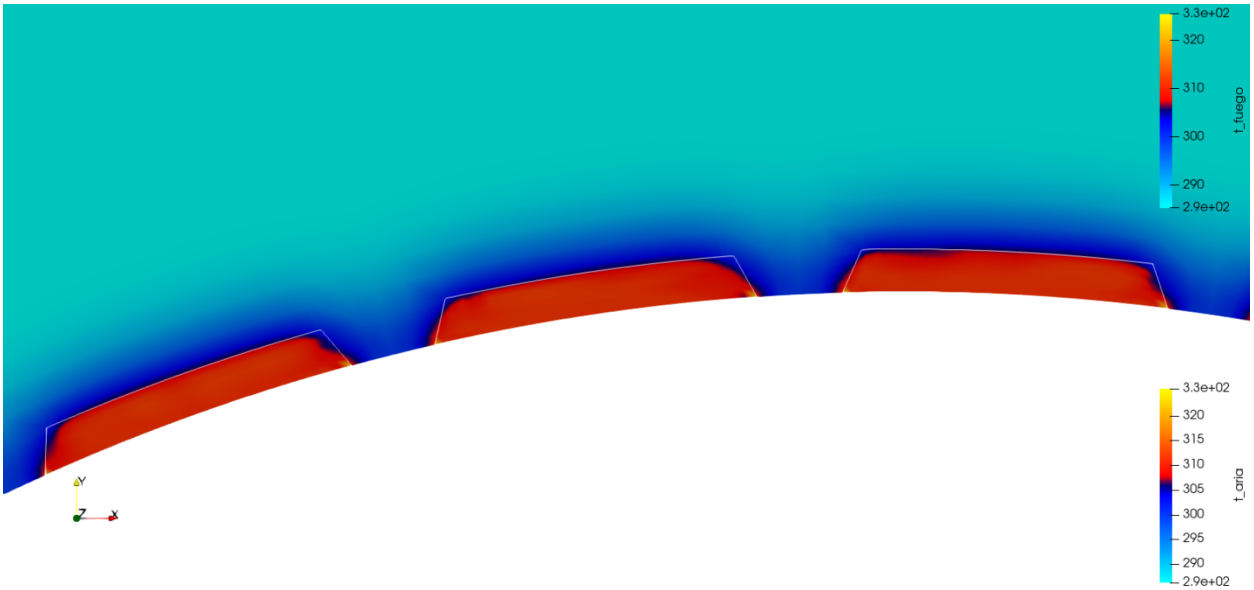

Figure 3-4. Fuego vs. Aria computational temperature range.

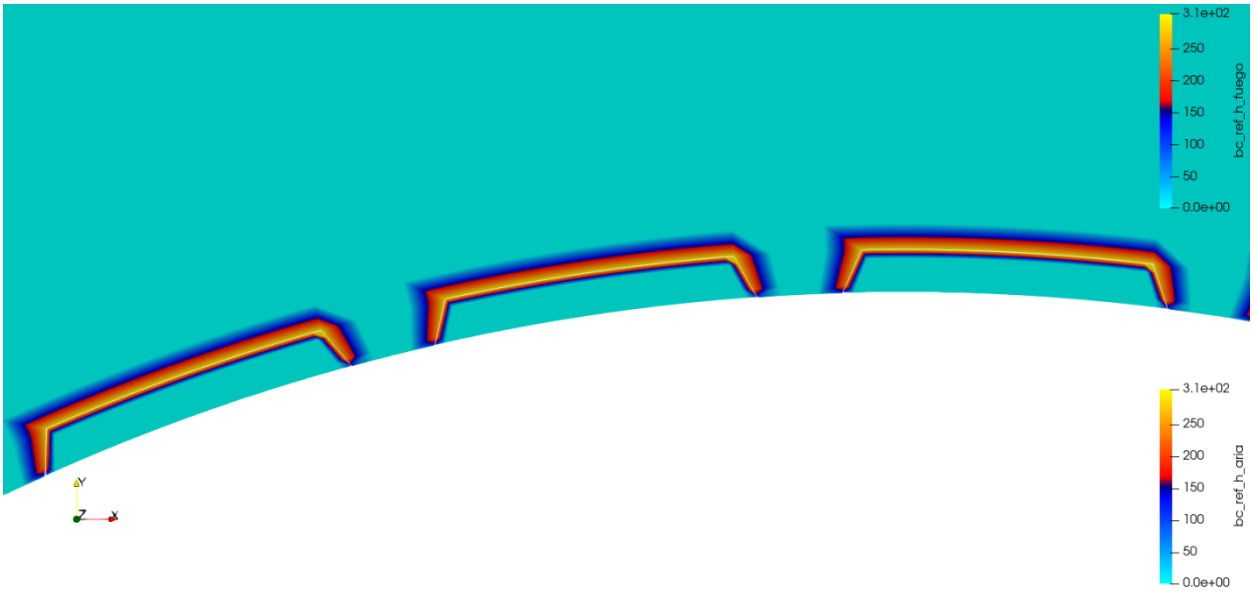

Figure 3-5. Fuego vs. Aria convective heat transfer coefficient range.

The temperature IC for the ground was variously imposed as a constant value or a gradient. The intent with the imposition of a temperature gradient was to begin the simulation with the ground temperature at steady state. In both cases, the outer wall of the ground was fixed at a temperature of 55.5 °F (286.2 K). The temperature gradient was determined by assuming the heat flux was bounded by a temperature of 125 °F (324.8 K) on the internal wall (the hot fluid temperature) and a temperature of 55.5 °F (286.2 K) for the outer wall.

Note that the problem with the above configuration is that it forced a heat flux based on an *arbitrary radius* chosen for the ground domain, which then affected how much heat flux was transferred across the boundary. Therefore, such approach created an artificial steady-state condition that was not supported by a sound technical basis. As a result, it was determined to begin with the entire ground at the cold temperature and allow the heat to diffuse through the ground volume. While this simulation did not reach steady state, it still provided an opportunity to model the heat flux, because the heat flux through the entire system is at a constant time-averaged value once the flow in the system reaches steady state. That is, the fluid time constant required to reach a steady-state time-averaged value is significantly faster than the time constant required to reach the thermal steady state. This assumption was confirmed, and is described later on in this section, by estimating the conduction heat transfer time-constant and comparing it against the computational output shown in Figure 3-6, which shows the Multiphysics normalized heat flux as a function of time. As expected, the heat flux quickly reached a steady state value, which was within 40 s of transient time for this situation.

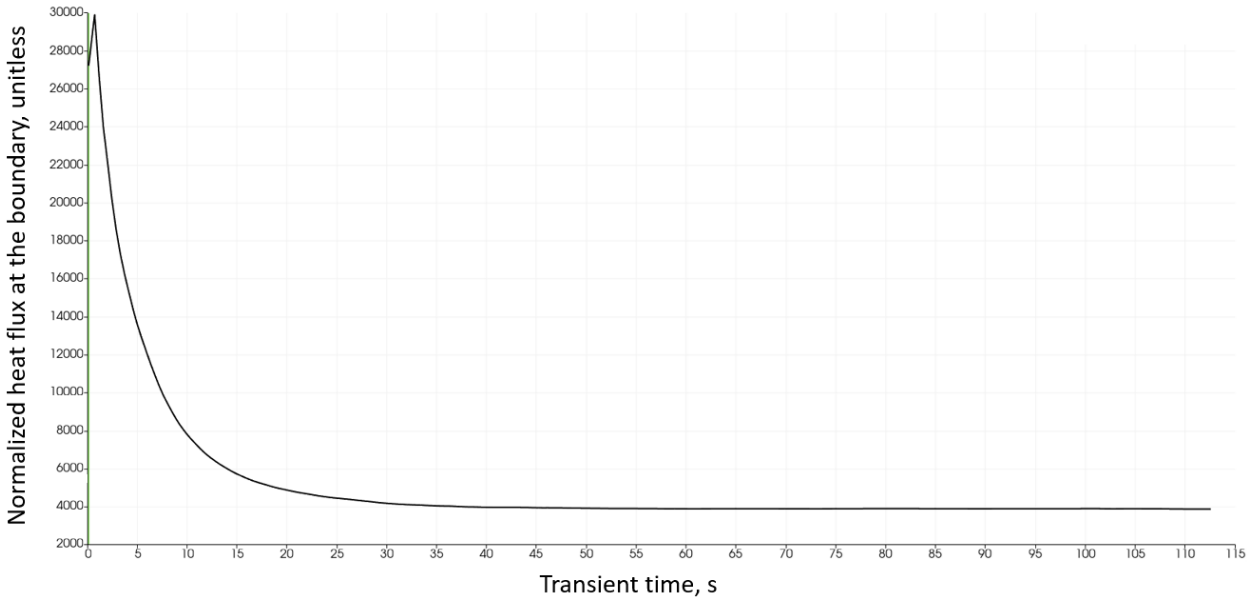

Figure 3-6. Multiphysics-calculated transient heat flux.

Nevertheless, though the analysis of the Multiphysics output showed that the fluid dynamics and heat transfer models worked properly, the computational time-stepping occurred at a very slow pace. To compensate for the slow pace, the number of parallel processors was increased. However, the data transfer time between the parallel computational regions ultimately slowed down the computational time to an unacceptable level. That is, as with any parallel computation, there is an optimal number of processors for any given computational model. In this case, 2,400 processors were optimal. Ironically, the computing resources available at SNL allowed for the usage of at least a factor of 100 times more processors, but using more processors slowed down the total computational time; likewise, using fewer than 2,400 processors also slowed down the total computational time. This is based on the well-known relationship that computational speed-up for a parallel system is approximately N*log(N), where N is the number of parallel processors. Thus, while the usage of more processors decreases the computational time, such N*log(N) gain is more than off-set by the excessive time usage required to share the computed data across the N processors.

Hence, for the Multiphysics case, raw computational power is not sufficient under these conditions. Fortunately, there are a number of methods to resolve this impasse. One approach is to take the heat flux that was computed by the Multiphysics approach and use it as a well-fought-for bona fide BC for the heat flux for usage in the stand-alone CFD calculation that now includes the proper heat flux BC that allows for significantly-faster computation. Another approach is to use the Multiphysics heat flux as a boundary for heat conduction PDEs that can then be solved analytically for the soil temperature distribution.

Both the stand-alone CFD and analytical approaches were employed successfully and are described next in Sections 3.2 and 3.3, respectively.

3.2. Stand-Alone CFD Model with Multiphysics Heat Flux Boundary

The fluid region physics was computed as a relatively fast-running stand-alone CFD model to investigate the turbulence characteristics. A side view of the fluid domain is shown in Figure 3-7, while Figure 3-8 shows the top view. The interface was defined as a wall with a fixed temperature of 109.1 °F (316 K), which was the approximate average after running the dimple-free Multiphysics model for approximately 508 s. Note that this does not represent a steady-state value, but is the farthest run from the cold starting condition that was performed using the Multiphysics model.

Figure 3-7. Side view of the dimpled heat exchanger.

Figure 3-8. Top view of the dimpled heat exchanger.

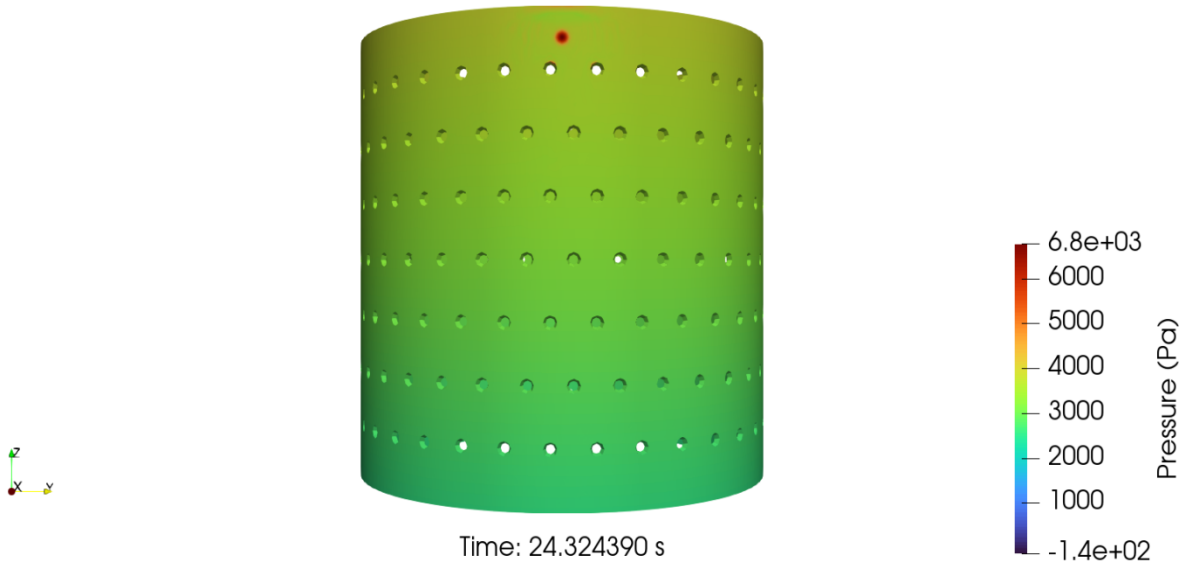

Figure 3-9. Stand-alone CFD simulation showing the calculated pressure distribution.

For this case, a 50-50 glycol/water solution was used, along with the Multiphysics-calculated heat flux as a closure BC. Figure 3-9 shows the pressure distribution, which essentially shows a sharp pressure drop as the working fluid enters the cylindrical shell. *After that, the shell experiences a minor pressure drop of about 1,000 Pa (0.15 psi) distributed across the entire cylindrical shell domain. This indicates that a small pump can very likely provide the forced flow necessary to move the coolant through the heat exchanger.* Figure 3-10 shows the fluid velocity distribution through the heat exchanger. The simulation clearly shows the eddies and flow pathways associated with turbulent flow. *It is noted that the upper half has a velocity distribution that ranges primarily from 0.1 to 1.5 m/s, while the bottom half shows a velocity distribution that is easily 1/10th the size. This indicates that a higher mass flow rate through the heat exchanger will significantly increase the amount of heat transfer, so long as the heat is removed fast enough by the ground. The heat transfer capacity of the ground has not been investigated in this report, and this is highly recommended for a future phase.* Finally, Figure 3-11 shows the temperature distribution across the cylindrical heat exchanger. The same pattern as the fluid distribution is noted again, with a very close 1:1 correspondence between the velocity and temperature distribution—the turbulent natural circulation causes an under-utilization

of the heat exchanger heat transfer cooling capacity, which can likely be remedied using a forced turbulent circulation flow, such as that provided by a pump.

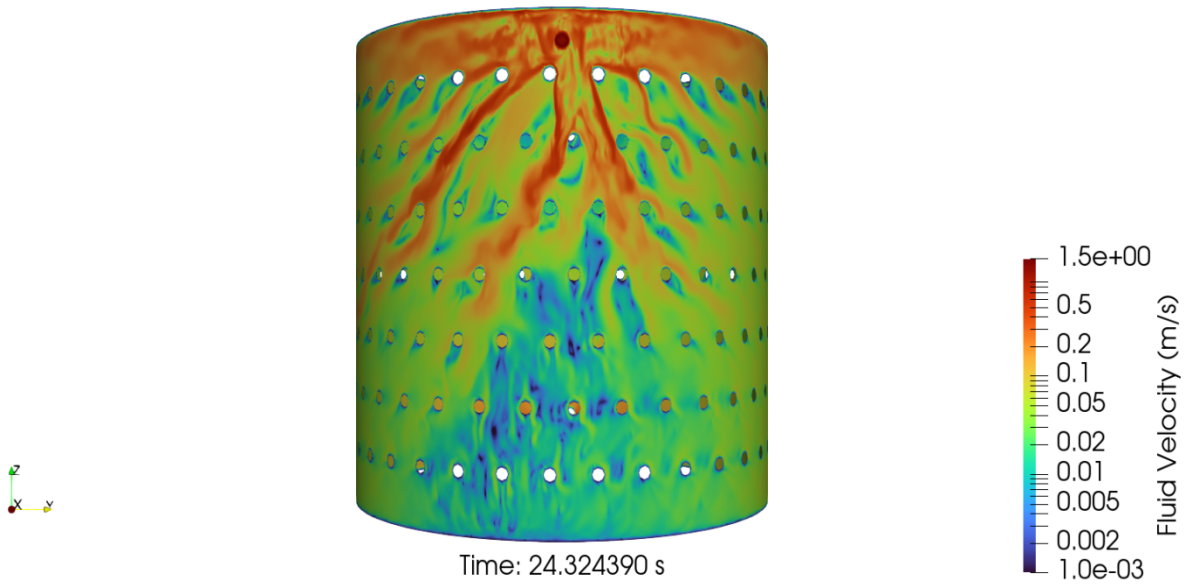

Figure 3-10. Stand-alone CFD simulation showing the calculated fluid velocity distribution.

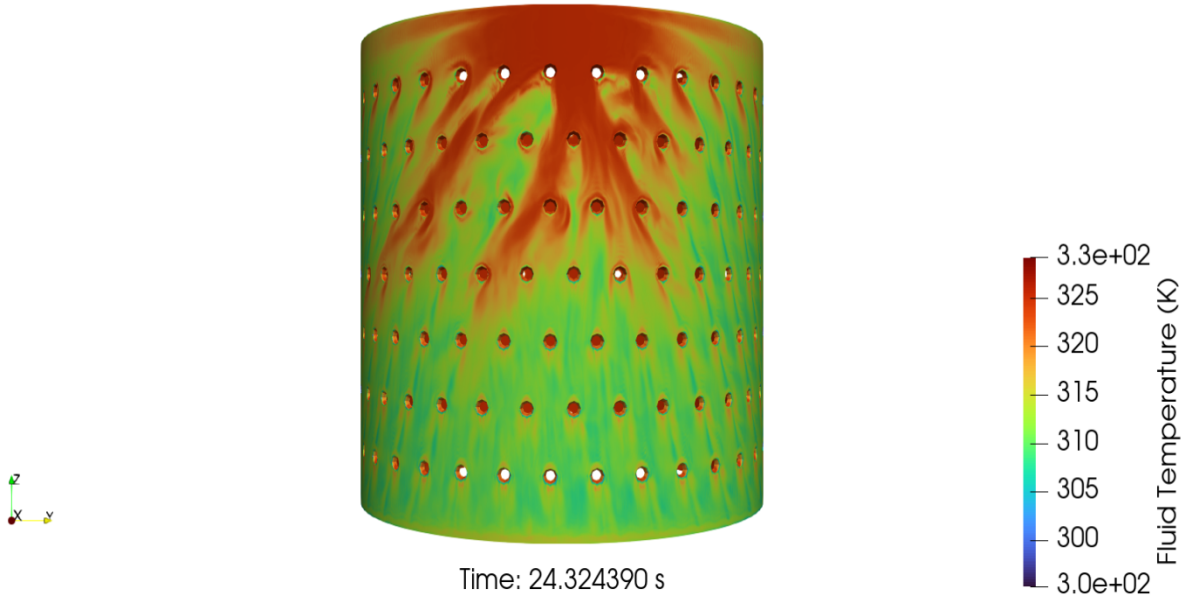

Figure 3-11. Stand-alone CFD simulation showing the calculated fluid temperature distribution.

3.3. Soil Temperature Distribution Based on Analytical Heat-Conduction Solutions

First, note that the time constant to conduct the heat radially outward through the soil can be estimated by performing a linear approximation for the heat conduction equation. Consider the transient conduction with no heat source. Then,

$$(1)\ \rho C_p \frac{\partial T}{\partial t} = k\frac{1}{r}\frac{\partial}{\partial r}\left(r\frac{\partial T}{\partial r}\right) = k\frac{1}{r}\left(r\frac{\partial^2 T}{\partial r^2} + \frac{\partial T}{\partial r}\right) = k\frac{\partial^2 T}{\partial r^2} + k\frac{1}{r}\frac{\partial T}{\partial r}$$

For small changes in temperature with respect to space and time, that is, linear changes, the partial derivatives can be approximated as,

$$(2)\ \begin{cases} \partial T \to \Delta T \\ \partial t \to \Delta t \\ \partial r \to \Delta r \\ r \to \Delta r \\ \dfrac{\partial^2 T}{\partial r^2} \to 0 \end{cases}$$

Note that $r \to \Delta r$ because only small changes in space are considered. Moreover, if ΔT is linear, then its second derivative with respect to *r* must be zero. Therefore, Equation 1 reduces as follows,

$$(3)\ \rho C_p \frac{\Delta T}{\Delta t} \sim k\frac{1}{\Delta r}\frac{\Delta T}{\Delta r}$$

Simplifying,

$$(4)\ \frac{1}{\Delta t} \sim \frac{k}{\rho C_p}\frac{1}{(\Delta r)^2} = \frac{\alpha}{(\Delta r)^2}$$

Hence,

$$(5)\ \Delta t \sim \sqrt{\frac{(\Delta r)^2}{\alpha}}$$

Though derived for small, linear changes, the temperature gradient across the ground is relatively slow with respect to the radial coordinate *r*, as already shown in Figure 3-11; and the same can be said of its change with respect to time.

For example, to propagate the conducted heat across a domain of 1.0 and 5.0 m radially away from the heater through soil with a thermal diffusivity of $3.42\text{x}10^{-7}$ m^2/s, takes 1,710 and 8,550 s, respectfully:

$$\Delta t \sim \sqrt{\frac{(\Delta r)^2}{\alpha}} = \sqrt{\frac{(1.0\ m)^2}{3.42\text{x}10^{-7} m^2/s}} = 1{,}710\ \text{s}$$

$$\Delta t \sim \sqrt{\frac{(\Delta r)^2}{\alpha}} = \sqrt{\frac{(5.0\ m)^2}{3.42\text{x}10^{-7} m^2/s}} = 8{,}550\ \text{s}$$

Clearly, a 1.0 m ground domain is computable via the high-performance parallel computers at SNL, as reaching ~1,700 s of transient time can be achieved via multiple restarts. In particular, the SNL high performance system allows simulations to run for a maximum of 48 hours, due to queuing issues. In this case, the Multiphysics simulations advanced by about 100 to 200 s of transient time per submission. Depending on the degree of usage for the high performance system, each submitted simulation remains in the queue for about three days before it starts running. The calculations can be restarted at the end-time for the previous calculation, thereby extending the simulation time by another 100 to 200 s per restart. However, the heat conduction domain in the radial direction is much larger. For an assumed range of 5.0 m, which requires five times as much transient time, 8,550 s.

Thus, to achieve the 5.0 m domain, a total of 43 to 86 restarts would be required. Assuming no issues such as maintenance and software upgrade downtime, each simulation would require close to a week. *Therefore, a single simulation that reaches the 8,550 s conduction-time-scale requires 0.8 to 1.7 years to achieve. This is clearly not acceptable, especially when multiple sensitivity simulations are required, not to mention the limited duration for NMSBA projects.*

The above estimate shows why it was not possible to reach the steady state for the Multiphysics CFD/heat conduction models solved by the coupled Fuego/Aria codes.

Therefore, to expedite the numerical computations, key output from the coupled CFD/thermal simulation (e.g., the computed heat flux) was input into the stand-alone CFD model. This was done such that the computation took care of the heat conduction portion of the simulation via a prototypic BC; that is, the more prototypical BC effectively captured the conduction heat transfer at a much faster pace than the Multiphysics model. Indeed, by employing this technique, the computational results were significantly accelerated by a factor of approximately 10, while retaining a reasonable representation of the heat conduction.

Now that that heat conduction time constant is better understood, it is time to solve the heat conduction governing PDEs. Assuming a constant thermal conductivity, the transient energy transfer is modeled by the following cylindrical-coordinate PDE,

$$(6)\ \rho C_p \frac{\partial T}{\partial t} = k\frac{1}{r}\frac{\partial}{\partial r}\left(r\frac{\partial T}{\partial r}\right) + \dot{Q}'''$$

Rather than the transient state, it is the steady state conduction of the heat that is of importance for the system. This greatly simplifies the above PDE, allowing its conversion to an ordinary differential equation,

$$(7A)\ \cancel{\rho C_p \frac{dT}{dt}} = k\frac{1}{r}\frac{d}{dr}\left(r\frac{dT}{dr}\right) + \dot{Q}'''$$

$$(7B)\ \frac{1}{r}\frac{d}{dr}\left(r\frac{dT}{dr}\right) = -\frac{\dot{Q}'''}{k}$$

The above equation can be integrated once to obtain

$$(7C)\ \int_{R_1}^{R_2}\frac{d}{dr}\left(r\frac{dT}{dr}\right)dr = -\frac{\dot{Q}'''}{k}\int_{R_1}^{R_2} r dr$$

$$(7D)\ r\frac{dT}{dr} = -\frac{\dot{Q}'''}{2k}r^2 + C_1,$$

which can be simplified by dividing by *r*

$$(7E)\ \frac{dT}{dr} = -\frac{\dot{Q}''' r}{2k} + \frac{C_1}{r}$$

Then, integrating one more time with respect to *r*,

$$(7F)\ \int\frac{dT}{dr}dr = -\frac{\dot{Q}'''}{2k}\int r dr + C_1\int\frac{1}{r}dr$$

The solution is

$$(8A)\ T(r) = -\frac{\dot{Q}'''}{4k}r^2 + C_1\ln(r) + C_2$$

which is subject to a specific solution once the C1 and C2 constants are defined. This is done by specifying two BCs that are specific to this problem. Thus, the C_1 and C_2 constants are evaluated by selecting steady-state BCs whereby

- *BC 1:* $T(R_1) = T_1$ (the temperature at the inner surface is specified at the surface's inner radial distance, R_1)

and

- *BC 2: $T(R_2) = T_2$* (the temperature of the ground at a distance R_2 is sufficiently away from the heat exchanger. This is selected as the radial distance that is sufficiently far away such that the ground temperature is essentially unchanged.

Substituting in those values, and after some algebra,

$$(8B)\ C_1 = \frac{\left(T_2 - T_1\right) + \frac{\dot{Q}'''}{4k}\left(R_2^2 - R_1^2\right)}{\ln\left(R_2 / R_1\right)}$$

$$(8C)\ C_2 = T_2 + \frac{\dot{Q}''' R_2^2}{4k} - C_1 \ln\left(R_2\right) = T_2 + \frac{\dot{Q}''' R_2^2}{4k} + \frac{\ln\left(R_2\right)}{\ln\left(R_2 / R_1\right)}\left[\left(T_2 - T_1\right) + \frac{\dot{Q}'''}{4k}\left(R_2^2 - R_1^2\right)\right]$$

If there is no heat source, then the above solution simplifies further to the set of Equations 9A through 9C:

$$(9A)\ T\left(r\right) = C_1 \ln(r) + C_2$$

$$(9B)\ C_1 = \frac{T_2 - T_1}{\ln\left(R_2 / R_1\right)}$$

$$(9C)\ C_2 = T_2 - C_1 \ln\left(R_2\right) = T_2 - \frac{\left(T_2 - T_1\right)\ln\left(R_2\right)}{\ln\left(R_2 / R_1\right)}$$

The heat conducted through a given material, e.g., the stainless-steel shell or the soil, can be obtained by taking the derivative of Equation 9A, as follows

$$(10)\ q_{cond} = -kA\frac{dT}{dr} = -kA\left(\frac{C_1}{r}\right) = -2\pi rLk\left(\frac{C_1}{r}\right) = -2\pi Lk\frac{\left(T_1 - T_2\right)}{\ln\left(R_1 / R_2\right)}.$$

The issue with the solutions found in Equations 9A-C and 10 is that they rely on the designation of the temperature magnitude of the ground at a somewhat arbitrary position. However, such uncertainty goes away if the experimental data from Section 2-2 is applied, though in the radial direction in this case. This implies that radially, the temperature will not change significantly past 9 to 12 feet (2.74 to 3.66 m) away from the heat exchanger, and moreover, that it hovers at approximately 63 °F (290.4 K). More specifically,

- *BC 2 based on experimental data:* $T(R_2) = T_2$, or *T(9 to 12 feet)* $= T_2 = 63$ °F; converted to SI units, this is *T(2.74 to 3.66 m)* $= T_2 = 290.4$ K.

Moreover, the results of the Aria code, when combined with Equations 5, 9A, 9B, 9C, and 10, provided a reasonable description of the entire system behavior. In particular, the Aria output allowed the application of improved BCs suitable for the thermal BCs used by the standalone CFD calculations. That is, the Aria simulation was run long enough to demonstrate that the heat flux that was conducted from the outer shell to the ground, reached a steady state value, as shown in Figure 3-6. This value can now be used to improve the heat BC of the CFD simulations. Hence, because the CFD simulations run much faster than the Aria simulations, reasonable modeling of the soil and heat exchanger were conducted at a much faster pace by employing part of the Aria output as boundary input for the Fuego CFD simulations. Alternatively, the second BC can also be pinned down by employing the soil temperature experimental data. So, whether the final BC is obtained computationally or experimentally, the result is that this information can now be used to compute the temperature gradient in the ground, from the heat exchanger outer radius, up to radius $r = 3.77$ m, where the temperature of the soil approaches its asymptotic value.

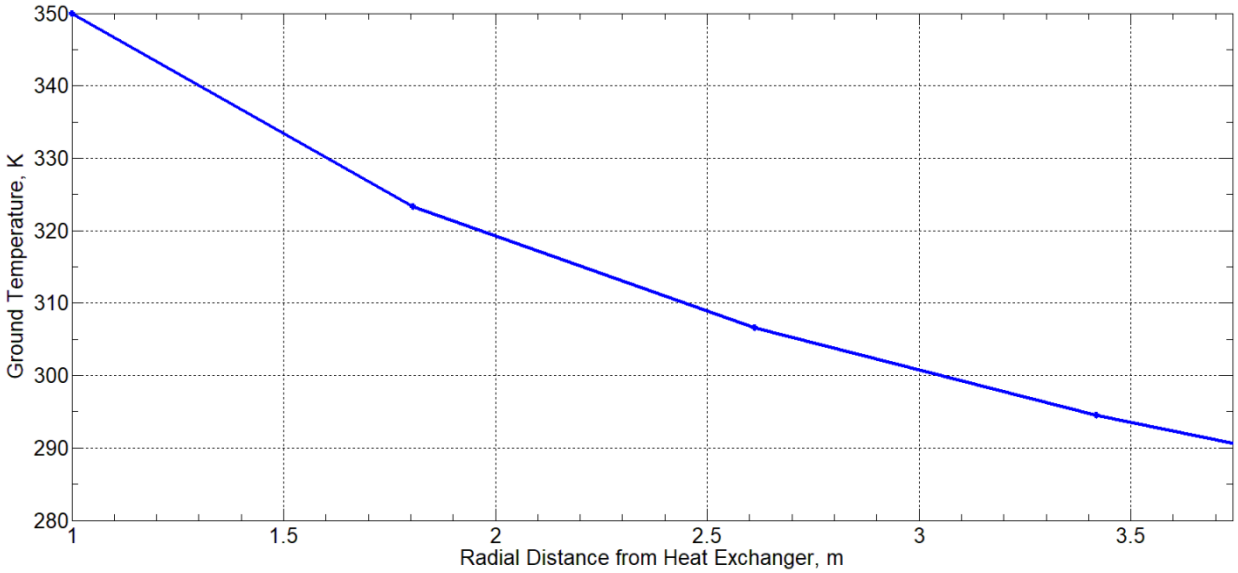

Figure 3-12. PDE solution for the soil temperature distribution as a function of radial distance *r*.

4. MISCELLANEOUS RECOMMENDATIONS REGARDING CORROSION AND TURBULENT FORCED FLOW VS. NATURAL CIRCULATION

Two additional issues are considered in this section: corrosion and circulation modes under turbulence. Section 4.1 considers corrosion issues associated with glycol, while Section 4.2 considers the replacement of natural circulation with forced circulation.

4.1. Recommendations to Reduce Corrosion

Corrosion can be a key factor affecting not only the efficiency of the heat exchanger, but also its usable lifetime.

Propylene glycol is considered corrosive to many alloys, so the usage of chemical inhibitors is highly recommended [Corrosionpedia, 2022]. In particular, glycol can oxidize, thereby forming organic acids. This can be prevented by adding chemical inhibitors. However, those compounds must be considered with regards to health and safety issues. *An easier approach is to simply flush out the glycol every so often, to reduce its acidic level. The degree of acidity can be easily measured using a pH meter.* Perhaps only flushing once a year would be necessary; this should be addressed in the near future. *In addition, reducing the amount of air in the vessel will reduce the amount of oxygen available to oxidize the glycol; gently tapping the sides of the exchanger with a plastic mallet might help purge some of the trapped air, as well as feed and bleed.*

In addition, the exterior of the innermost surface of the heat exchanger can be coated with a varnish or plastic coating to inhibit corrosion, as such surface does not contribute much towards heat transfer once steady state is reached. By contrast, the outermost heat exchanger surface will be in contact with soil containing water and oxygen, which will eventually build a corrosive layer that acts as a thermal barrier that can severely reduce its thermal performance. *The usage of strategically-positioned sacrificial anode rods may reduce such corrosion.*

4.2. Recommendations Regarding Forced vs. Natural Circulation

The work presented up to this point considers a flow induced by natural circulation, whereby a wall structure, such as a house or greenhouse, provides a temperature gradient across a fluid, thereby inducing flow. Though passive, the flow has limitations. To investigate this, consider the driver for natural circulation, the Grashof number (*Gr*).

For natural circulation flows, that is, the motion of a fluid based on temperature gradients, *Gr* determines the degree of convection heat transfer. In this case, the fluid moves through the system as a result of the density differences. *Gr* times the Prandtl number (*Pr*) is a measure of the degree of laminarity or turbulence under natural circulation, where *GrPr* = Rayleigh number = *Ra* [Holman, 1990; Rodriguez, 2019]. *Gr* is defined as,

$$(11)\ Gr = \frac{\beta g h^3 \Delta T}{\nu^2}$$

where

$\Delta T = \left(T_w - T_\infty\right)$,

$T_w =$ wall temperature,

T_∞ = fluid temperature far away from the heat transfer wall,

β = fluid volume expansion coefficient,

g = gravitational constant,

and

h = system characteristic height.

For turbulent natural circulation flows over a vertical plate [Holman, 1990], the amount of turbulent heat transfer is expressed via the Nusselt number (*Nu*),

$$(12)\ Nu_{nat,tur} = 0.1\left(GrPr\right)^{1/3}$$

Ironically, though it is the linear temperature gradient ΔT that induces the flow, the degree of natural circulation is a strong function of the system height being heated by the sun, to the power of three.

For pumped (forced convection) flows, it is the Reynolds number (*Re*) that determines the relative impact of turbulence and heat transfer, which is defined as,

$$(13)\ Re = \frac{x_{char} u_{char} \rho}{\mu} = \frac{x_{char} u_{char}}{\nu}$$

where

$x_{char} =$ flow channel characteristic length,

u_{char} = fluid characteristic velocity,

ρ = fluid density,

μ = fluid dynamic viscosity,

and

$\nu = \frac{\mu}{\rho} =$ fluid kinematic viscosity.

For turbulent, forced flow heat transfer, the equivalent expression is

$$(14)\ Nu_{for,tur} = 0.023 Re^{0.8} Pr^{0.3}$$

So now, the following premise is made: what information can be gleaned if the turbulent forced circulation were greater than the turbulent natural circulation? From a mathematical point of view, this can be more formally written as a comparison of the heat transfer involving *Nu*,

$$(15A)\quad Nu_{for,tur} > Nu_{nat,tur}$$

or

$$(15B)\quad 0.023Re^{0.8}Pr^{0.3} > 0.1\left(GrPr\right)^{1/3}$$

To simplify, $Pr^{0.3}$ cancels out $Pr^{1/3}$ and solving for *Re*,

$$(16)\quad Re > \left(\frac{0.1}{0.023}Gr^{1/3}\right)^{\frac{1}{0.8}} = 5.43Gr^{0.417}$$

It is also well-known that laminar natural circulation transitions to turbulent flow for $5\text{x}10^8 \leq Gr \leq 1\text{x}10^9$. Substituting both of these numbers indicates that *Re* > 23,000 to 30,750, which seems high by a factor of five or so. However, this is a first order estimate, which usually falls within a factor of 10 or less. Moreover, the value for *Gr* grows as a function of height for this system, while *Re* remains constant.

5. SUMMARY, CONCLUSIONS, AND RECOMMENDATIONS

For this phase, it was desired to 1) obtain more prototypic modeling of the soil, 2) couple the CFD and heat conduction models, 3) apply more mechanistic heat transfer BCs, and 4) obtain more detailed system behavior dynamics and performance of the heat exchanger and the soil system. Upon applying diverse solution methods that included stand-alone CFD, Multiphysics (CFD coupled with heat conduction), experiments, and PDE solutions, the following recommendations, findings, and points are noted:

- The heat exchanger should be placed in a region with a low caliche concentration.
- The benefit of reduced temperature beyond a 9- to 12-foot cavity is counterproductive.
- During the summertime period, the lowest operational temperature for the heat exchanger is approximately 65.5 to 67.5 °F (291.8 to 292.9 K).
- The ground near the heat exchanger can be shaded to increase the performance of the heat exchanger.
    - ✓ This can be achieved via a porch-like structure, or more simply, via a solar-reflective blanket placed on top of the soil.
- The heat exchanger shell experiences a minor pressure drop of about 1,000 Pa (0.15 psi) distributed across the entire cylindrical shell domain.
    - ✓ Therefore, a small pump can likely provide the forced flow necessary to move the coolant through the heat exchanger.
- The upper half of the heat exchanger has a velocity distribution that ranged mostly from 0.1 to 1.5 m/s, while the bottom half showed a velocity distribution that was $1/10^{th}$ the magnitude.
    - ✓ This indicates that a higher mass flow rate through the heat exchanger can significantly increase the amount of heat transfer, so long as the heat is removed fast enough by the ground. (This provides an argument for forced circulation.)
- The heat transfer capacity of the ground was not investigated in this report and is highly recommended for a future phase.
- Soil temperature experimental data and the heat flux obtained via the Multiphysics simulations each provided an independent BC that enabled the proper treatment of the soil model.
- Propylene glycol is considered corrosive to many alloys.
    - ✓ Corrosion can be prevented by adding chemical inhibitors, pH control, regular flushing, tapping out the trapped air, and feed and bleed.
    - ✓ Due to its simplicity, flushing is recommended.
- The exterior of the innermost surface of the heat exchanger can be coated with a varnish or plastic coating to inhibit corrosion.
- Strategically-positioned sacrificial anode rods may reduce corrosion on the outermost heat exchanger surface.
- Usage of a small pump that generates *Re* greater than approximately 4,600 will likely result in more heat transfer than if turbulent natural circulation were employed.

6. REFERENCES

Abu-Hamdeh, N. H. and R. C. Reeder, “Soil Thermal Conductivity: Effects of Density, Moisture, Salt Concentration, and Organic Matter”, Soil Sci. Soc. Am. J., Vol 64, 2000.

DPGS, “Dynalene Propylene Glycol Series”, PG Engineering Guide, Dynalene, Inc., 2014.

ASTM, “Standard Test Method for Determination of Thermal Conductivity of Soil and Rock by Thermal Needle Probe Procedure”, ASTM International, Designation: D5334-22.

Corrosionpedia, “Propylene Glycol”, https://www.corrosionpedia.com/definition/2777/propylene-glycol. Accessed on September 15, 2022.

“ETB, Engineering ToolBox, “Propylene Glycol based Heat-Transfer Fluids”, https://www.engineeringtoolbox.com/propylene-glycol-d_363.html. Accessed on April 24, 2020.

GHTF, “Glycol Heat-Transfer Fluids Ethylene Glycol versus Propylene Glycol”, http://www.veoliawatertech.com/crownsolutions/ressources/documents/2/21823,Glycol.pdf. Accessed on April 24, 2020.

Holman, J. P., *Heat Transfer*. McGraw-Hill, Seventh Edition, New York, 1990.

Khattab, I. S. et al., “Density, viscosity, surface tension, and molar volume of propylene glycol + water mixtures from 293 to 323 K and correlations by the Jouyban–Acree model”, Arabian Journal of Chemistry, Vol. 10, 2017.

Loam, Wikipedia “Loam”, https://en.wikipedia.org/wiki/Loam. Accessed on May 15, 2020.

Melinder, A., “Properties of Secondary Working Fluids (Secondary Refrigerants or Coolants, Heat Transfer Fluids) for Indirect Systems”, International Institute of Refrigeration, France, 2010.

Melinder, A., “Thermophysical Properties of Aqueous Solutions Used as Secondary Working Fluids”, PhD Thesis, Division of Applied Thermodynamics and Refrigeration, Royal Institute of Technology, Sweden, 2007.

Ouzzane, M., P. E.-Nejad, Z. Aidoun, and L. Lamarche, “Analysis of the Convective Heat Exchange Effect on the Undisturbed Ground Temperature”, Solar Energy, Vol. 108, pp. 340-347, 2014.

PEX, “Cross-Linked Polyethylene”, Wikipedia, https://en.wikipedia.org/wiki/Cross-linked_polyethylene. Accessed on May 13, 2020.

Rodriguez, S., *Applied Computational Fluid Dynamics and Modeling—Practical Tools, Tips, and Techniques*, Springer Publishing, 2019.

Rodriguez, S., G. Monroe, and Jennifer Fort, “Dimpled Heat Exchanger CFD and Heat Transfer Design and Analysis”, Sandia National Laboratories, 2020.

Sun, T. and A. S. Teja, “Density, Viscosity and Thermal Conductivity of Aqueous Solutions of Propylene Glycol, Dipropylene Glycol, and Tripopylene Glycols between 290 K and 460 K”, J. Chem. Eng. Data, Vol. 49, 2004.

TPPI, “R-Value and Thermal Conductivity of PEX and PE-RT”, The Plastics Pipe Institute, Inc., TR-48/2014, 2014.

WEBA, “Glycol-Based Heat Transfer Fluid Technical Manual”, WEBA Technology Corp., http://www.webacorp.com/HTF-Manual.pdf, 2003.

Wilcox, D. C., *Turbulence Modeling for CFD*, 3rd Ed., DCW Industries, Inc., 2006.

DISTRIBUTION

Email—Internal

Name	Org.	Sandia Email Address
John Martinez	01983	jmart30@sandia.gov
Technical Library	01977	sanddocs@sandia.gov

Email—External

Name	Company Email Address	Company Name
Patrick Johnson	newmexicokid@gmail.com	C Johnson Development

This page left blank

This page left blank

Sandia National Laboratories

Sandia National Laboratories is a multimission laboratory managed and operated by National Technology & Engineering Solutions of Sandia LLC, a wholly owned subsidiary of Honeywell International Inc. for the U.S. Department of Energy's National Nuclear Security Administration under contract DE-NA0003525.